Quantitative model for the change of optical resonance in neural activity detection systems based on surface plasmon resonance

Seung Ho Choi [a], Sung June Kim [a,b], Chang-Hwan Im [c], Shin Ae Kim [b], Daejoong Kim [d,*]

[a] Interdisciplinary Program of Bioengineering, Seoul National University, Seoul, Republic of Korea
[b] School of Electrical Engineering, Seoul National University, Seoul, Republic of Korea
[c] Department of Biomedical Engineering, Yonsei University, Wonju, Republic of Korea
[d] Department of Mechanical Engineering, Sogang University, Seoul, Republic of Korea

ARTICLE INFO

ABSTRACT

The mechanism of neural activity detection using the surface plasmon resonance (SPR) phenomenon was theoretically explored in this paper. Investigating the mechanism of SPR neural recordings has been difficult due to the complex relationship between different physiological and physical processes such as excitation of a nerve fiber and coherent charge fluctuations on the metal surface. This paper examines how these different processes may be connected by introducing a set of compartmental theoretical models that deal with the molecular scale phenomena; Poisson–Boltzmann (PB) equation, which was used to describe the ion concentration change under the time varying electrostatic potential, Drude–Lorentz electron model, which was used to describe electron dynamics under the time varying external forces, and a Fresnel's three-layered model, which expresses the reflectivity of the SPR system in terms of the dielectric constants. Each physical theoretical model was numerically analyzed using the finite element method (FEM) formulated for the PB equation and the Green's method formulated for the Drude–Lorentz electron equation. The model predicts that the ionic thermal force originating from the opening of the K^+ ion channel is fundamental for modifying the dipole moment of the gold's free electron; thus, the reflectivity is changed in the SPR system. The discussion was done also on important attributes of the SPR signal such as biphasic fluctuation and the electrical noise-free characteristics.

© 2010 Elsevier Ltd. All rights reserved.

1. Introduction

Neurons have attracted a significant amount of interest and research over the past centuries. To better understand the nature of neurons, researchers across a wide range of disciplines have conducted a great number of experimental and theoretical studies. Surface plasmon resonance (SPR) [1–3] is a relatively new optical method and has been used to detect electrically stimulated neural activity using reflected TM-polarized light from a thin gold film that is closely attached under the neuron. Kim et al. [4] used a conventional Kretschmann SPR configuration to detect neural signals from rat sciatic nerve. In their work, they demonstrated that this method could be used as an artifact- and label-free technique, like other optical techniques which monitoring changes in birefringence, scattering and dielectric constant of neurons [5–14]. In addition, the detected SPR neural responses were so sensitive that signal averaging was not required.

However, the relationship between the extracellular potential and SPR neural signal has not yet been well established because the

characteristics of the two signals are completely different. The biphasic 1 mA current with 1 Hz and 1.5 ms pulse duration (see Fig. 1C) generates the electrical neural signal from rat sciatic nerve (see Fig. 1A) and the SPR neural signal (see Fig. 1B). As shown in Fig. 1, the significant differences of the SPR neural signal are as follows:

1. Biphasic oscillation.
2. Independence from electrical noise.

A theoretical framework for interpreting the mechanism of the SPR-based neural activity recording should be established to gain deeper insight into the mechanism of SPR neural activity detection and to use this technique in different applications such as SPR-based in vivo neural recording [15–18] and image acquisition of neural activity in cultured neural network [19–22]. Several near field and light transport theories have been used to successfully explain the experimental results of biomedical optics [23–32]; these physical theories thus may be able to explain the mechanism by which SPR detects neural activity. Recently, Zhang et al. [33] conducted the same experiment as Kim et al. [4] using a modified gold surface, which is part of the SPR neural recording system. They

---

also provided some theoretical explanation for the mechanism of SPR neural activity detection. They believed that the scattering change had a linear relation with the nerve's extracellular potential change. However, this explanation cannot explain the completely different characteristics of the SPR neural signal, especially the electrical noise-free characteristics. Under the Zhang et al.'s theory, a SPR signal should exist at the time as the electrical noise, which is associated with the nerve stimulation current.

Kume et al. [34,35] solved an electromagnetic problem, which may be applicable to the mechanism of SPR-based neural detection. In
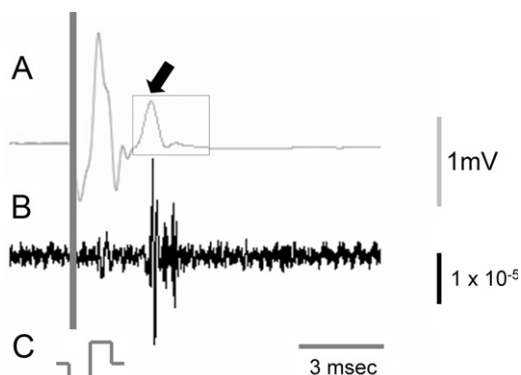

Fig. 1. (A) Electrically recorded neural activity and corresponding (B) SPR neural signal from rat sciatic nerve modulated by (C) 1 mA current stimulation, which was used as a template in the present work (kindly provided to us by Shin Ae Kim and Professor Sung June Kim, Nano-Bioelectronics and Systems Laboratory, Seoul National University). The arrow indicates the peak of the recorded extracellular potential and the electrical signal in the box was used as a boundary condition of the Poisson–Boltzmann equation.

their studies, they performed an electric field analysis for an isolated particle placed near a metal surface surrounded by dielectric medium. They calculated the electric field distributions around the particle and found that the resonant wavelength varies with the distance between the particle and surface. However, this single electric field analysis also has limitations; it does not account for the nonlinear characteristics of the SPR neural signal, the noise-like biphasic oscillation [4].

To fully understand the process of SPR-based neural detection, a set of different physical theories that encompass the dynamic process of SPR neural recording should be determined and interconnected with each other. The recorded signal is the change of reflectance ($\Delta 0R$) at a fixed angle (see Fig. 2B) when TM-polarized light is incident at a fixed angle as shown in Fig. 2A. When polarized light is passing through the prism in the Kretschmann configuration, the momentum of the light oscillates electrons on the gold surface, which generates surface plasmon (SP) waves [1]. The light is then reflected from the gold surface and its intensity or zeroth order reflectivity ($0R$) is determined by the dielectric constant of the surrounding medium. Fig. 2B shows how the reflectance curve (*dark line*) changes its resonant angle θ_{spr} when the real part of the dielectric constant of the gold layer changes by 10% from its original value. Therefore, an assumption can be made that the dielectric constant of one or several elements in Fig. 2A is modified by the electrophysiological process of the nerve fiber. The space close to the SPR system can be divided into three areas (nerve membrane; aCSF region; gold atoms) and a separate analysis is possible about how each area's dielectric constant has been changed.

The first assumption in this analysis is that the change in the nerve's dielectric constant will directly affect the change in $\Delta 0R$. Changes in the dielectric constant of electrically stimulated nerves have been previously studied by monitoring changes in the birefringence and scattering. In addition, the origins of these changes have
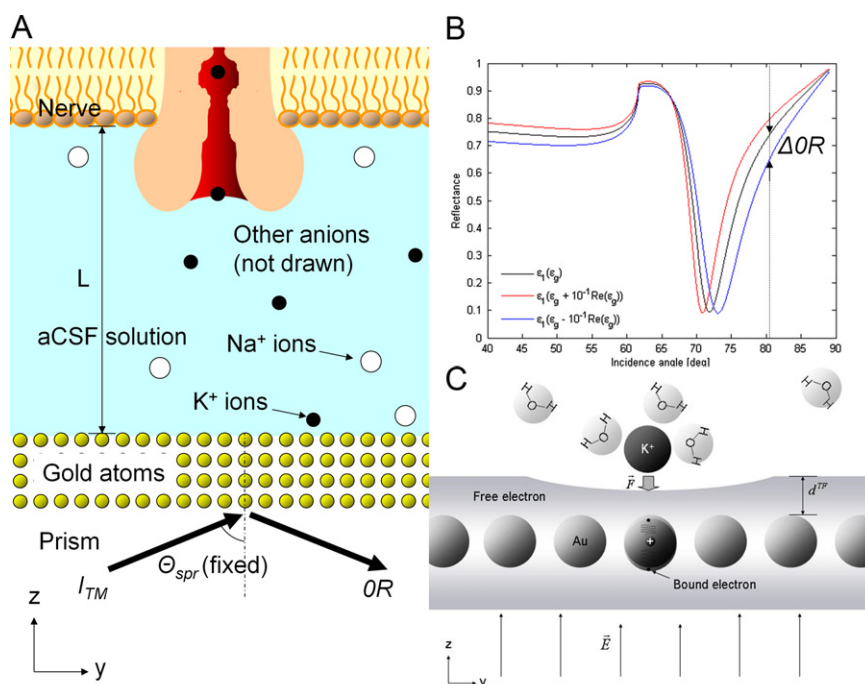

Fig. 2. (A) The two-dimensionally reduced model for a SPR neural recording system under TM-polarized light illumination with an incidence angle θ_{spr}. The nerve membrane was in close proximity (nanoscale distance L) to the gold film (modeled as a group of gold atoms), which had a thickness d and was coated on the prism substrate. The gap region was filled with aCSF fluid, which included only K^+ ions, Na^+ ions and water molecules (other anions were not included, see text). The two dimensional Cartesian coordinate system was used as displayed. (B) Calculated $0R$ when the incidence angle was varied from 0 to 90°. The dark line is the $0R$ curve using the original dielectric constant of gold. The red and blue lines represent the real part of the dielectric constant of gold layer when it changed by $+10\%$ and -10% relative to its original value, respectively. (C) Atomistic model system of a gold film under the external electric force $\vec{E}$, induced from the incidence of light, and ionic force $\vec{F}_{ion}$, induced from the collision of the hydrated ion. The gold layer includes a proton, bound electron, which was elastically bound to the proton, and free electron, which was localized in the z direction within the Thomas–Fermi screening length d^{TF}. We assumed that all external forces had only a z component. (For interpretation of the references to color in this figure legend, the reader is referred to the web version of this article.)

been studied and are proposed to be structural (e.g., reorganization of axon membrane protein molecules [5,6]) and transparent (e.g., changes in ionic concentration near the nerve membrane [9]) changes of the nerve cell, moreover, these hypotheses are still in controversy. These origins cannot explain the SPR signal because all of those experimental results show that the changes in the nerve's intrinsic optical properties are monophasic. The experimental $\Delta 0R$ should vary monophasically according to the first assumption, however.

Another possible assumption is that the change in the aCSF region's dielectric constant is a fundamental factor of the SPR signal. This assumption seems more reasonable than the first one because the thermal movement of several types of ions would generate the noise-like fluctuations in the dielectric constant of the aCSF region. However, the deviations in the aCSF dielectric constant during nerve excitation were less than 13.39×10^{-5}, which was estimated from the maximum ion distribution change in the aCSF region. The maximum ion distribution change will be discussed in more detail later. The change of $\Delta 0R$ from deviations in the aCSF dielectric constant is calculated and the computed $\Delta 0R$ change was 1.8×10^{-8}, which was negligible compare to that of the experimental result on the order of 1×10^{-5}.

Consideration of these aspects leads to the focus on the changes in the gold film's dielectric constant. Since the change of $\Delta 0R$ was found to be strongly dependent on the corresponding recorded extracellular potential (see Fig. 1B), the key factor affecting the dielectric constant of the nerve–gold interface was assumed to be the presence of counterions placed at a nanoscale distance from the gold film, which was mostly determined by the Na^+ and K^+ conductance of the nerve membrane [36]. Moreover, it is expected that ionic force originated from the thermal movement of counterions can be related to the biphasically oscillating noise-like reflectance signal, because the ion movement can modify the movement of free electron near the gold surface, which can affect the optical properties of the gold film. These assumptions are described in more detail in Section 2.

This paper presents a model on the dynamic interactions between the rat sciatic nerve and SPR. The effects of mechanical pressure on the motion of free and bound electrons of gold atoms were described using the Drude–Lorentz electron equation [37] and its solution was numerically computed using the Green's method [38]. In addition, the mechanical pressure was interpreted as the thermal force of the counterion, which depends on the concentration of counterions placed near the surface of gold atoms. Then, the change in reflectivity was obtained by solving the Fresnel's equation (function of dielectric constants) for the three layer system consisting of a dielectric (e.g., prism), metal film and dielectric medium (e.g., nerve which is immersed in the artificial cerebrospinal (aCSF) fluid) [1]. For the analysis of the distributions of counterions near the surface of gold atoms, a finite element method (FEM) [39] was formulated for the Poisson–Boltzmann (PB) equation [40,41]. The proposed hybrid approach was applied to the experimental results obtained by Kim et al. [4] and the characteristics of the measured SPR neural signals was numerically obtained such as biphasic oscillation and independence from electrical noise.

2. The multiphysical model for SPR detection of neural activity

This section presents models of the mechanisms for SPR based neural activity detection and the set of physical theories used in the model, which were numerically solved. A model system was constructed for a SPR neural recording setup, which is represented by a two-dimensional area. This area is schematically illustrated in Fig. 2A. The nerve membrane of rat sciatic nerve surrounded by aCSF solution is in closely close proximity (nanoscale distance L) to the Kretschmann attenuated total reflection (ATR) system, which

consists of a BK7 prism and a flat gold substrate with a thickness of d and the TM-polarized light is illuminated with an incidence angle θ_{spr} through the prism. Each area is described in the atomic scale; the masses and sizes of each element are summarized in Table 1. The aCSF solution contains more compounds than those listed in Table 1. The reason why only Na^+ ions and K^+ ions are included in the model will be discussed later.

In this model system, the main assumption is that the K^+ ions are fired out of the channel in a ballistic manner, forming a jet which imparts momentum to the gold surface. Therefore this section is organized as follows. First, the relationship between reflectance from SPR system and dielectric constant of gold film is described. Then, the hypothetical link between this optical property change of gold film and kinetic force of K^+ ion particle is presented. To distinguish these ballistic ions from the many others, an ad-hoc activity factor is multiplied into account for the fact that newly emitted ions are not yet hydrated. The dipole moment generated by this multiple ion impact would couple to the optical-frequency dipole moment which determines the optical refractive index/reflectivity. Finally, the theoretical reasons why the signal from thermal movement of cation could be separated from electrical noise in advance of SPR signal are discussed.

2.1. Calculation of the reflectance at three layer SPR system

When the TM-polarized light is incident on the prism–gold interface with a resonant angle θ_{spr}, most of the light is absorbed onto the gold surface to generate the SP and minimum $0R$. In the experiment, this reflected light was used to monitor the electrophysiological activity in the nerve. In the case of the Kretschmann ATR configuration, the $0R$ for TM-polarized light is given by the following equation borrowed from Fresnel [1]:

$$0R = \left| \frac{r_{01} + r_{12}\exp(2ik_z d)}{1 + r_{01}r_{12}\exp(2ik_z d)} \right|^2, \tag{1}$$

with

$$r_{ik} = \frac{\left(\frac{k_{zi}}{\varepsilon_i} - \frac{k_{zk}}{\varepsilon_k}\right)}{\left(\frac{k_{zi}}{\varepsilon_i} + \frac{k_{zk}}{\varepsilon_k}\right)}, \quad k_z = \sqrt{\varepsilon_i\left(\frac{\omega}{c}\right)^2 - k_x^2} \text{ and } k_x = \sqrt{\varepsilon_0}\frac{\omega}{c}\sin\theta_0. \tag{2}$$

Table 1
Sizes and masses of various components in the model system.

Elements in model system	Sizes [nm] and masses [M]
K^+ ion [52]	Atomic mass: 39.10 Crystal radius: 0.133 Hydration radius: 0.126
Na^+ ion [52]	Atomic mass: 22.99 Crystal radius: 0.098 Hydration radius: 0.185 (Spacing between K^+ and Na^+ ions in the aCSF solution (50): $\cong 1.7$)
Na^+ [58]	Molecular mass: 18.015 Molecular radius: 0.138
Au [59]	Atomic mass: 196.96 Atomic radius: 0.135
K^+ ion channel [54,60]	Channel height: 12 Channel diameter: 5 (Spacing between K^+ ion channels in the rat axon: $\cong 210$)
Cell membrane [61]	Thickness: 4

These sizes and masses of various components are considered to design the model system illustrated in Fig. 2A. The mass information is important to calculate the amplitude of ionic force in Eq. (8).

Eq. (1) can be derived by assuming that there are three layers (0 prism; 1 gold film; 2 aCSF fluid). Here, r_{ik} is the Fresnel reflection coefficient at an interface between i and k materials, k_z is the z component of the wave vector in the gold film, ε_i is the dielectric constant of the ith material, ω is the angular frequency of the incident light and c is the speed of light. The experimental wavelength λ of incident light was 635 nm [4]. The dielectric constants of the prism, gold and aCSF region at 635 nm were calculated or chosen from a dielectric constant database and were set to be 2.2958, $-11.85 + 1.21i$ [42,43] and 1.7788 (obtained from curve fit of the raw data of dielectric constants for aqueous solutions [44]), respectively.

2.2. Changes in the dielectric constant of gold film induced from ionic collision

The modeling was performed on the biphasically oscillating intensity of $\Delta 0R$ in Eq. (1) by investigating the change in the dielectric constant described in Eq. (2). Of all the dielectric constants of the media, the changes in the dielectric constant of the gold substrate were found to be a main parameter due to the thermal force of ion movement induced from the jet force of ion flow through an ion-channel. From the macroscopic point of view, the electric polarization $\overrightarrow{P}$ (dipole moment per unit volume) contributes to the generation of the electric displacement $\overrightarrow{D}$, $\overrightarrow{D} = \varepsilon_0 \overrightarrow{E} + \overrightarrow{P}$. Thus, the dielectric constant of gold, $\varepsilon / \varepsilon_0$, can be expressed as follows:

$$\frac{\varepsilon(\omega)}{\varepsilon_0} = 1 + \frac{|\overrightarrow{P}|}{\varepsilon_0 |\overrightarrow{E}|}, \text{ with } \overrightarrow{P} = N^{mol} \langle \overrightarrow{p}^{mol} \rangle, \tag{3}$$

where $\overrightarrow{E}$ is the external electric field, which varies in time with the angular frequency ω as $\overrightarrow{z} E_0 e^{-i\omega t}$, ε_0 is the dielectric constant of free space, N^{mol} is the number of molecules per unit volume and $\langle \overrightarrow{p}^{mol} \rangle$ is the average dipole moment of the molecule. The dipole moment of one electron is determined from the displacement of its equilibrium $\overrightarrow{r}$, $\overrightarrow{p} (= -e \overrightarrow{r})$, where e is the charge of the electron. A schematic diagram of the atomistic representation of the gold film under the net force is shown in Fig. 2C; the amplitude of oscillation is displayed unrealistically high for illustrative purposes. Since the outer electrons of gold atoms are weakly bound [45], electrons do not belong to a particular atom-atom bond and they form an electron cloud or plasma (highly concentrated free electrons about 10^{23} cm^{-3} [1]), which is localized within the Thomas–Fermi screening length d^{TF} (see Fig. 6A). An electromagnetic wave $\overrightarrow{E}$ with angular frequency ω forces the free electrons and the bound electrons of the gold atoms into an oscillatory motion that has the same frequency as that of the electromagnetic wave [46]. Therefore, the displacement of the bound and the free electron from its equilibrium position contributes to the average dipole moment of the molecule [47]. To account for the elastic motion of bound and free electrons due to electromagnetic and mechanical forces, the electrons in the model were approximated in terms of individual harmonic oscillators, through the following modified electron model [37]:

$$m^e \left[\frac{\partial^2 z^e(t)}{\partial t^2} + \gamma \frac{\partial z^e(t)}{\partial t} + \omega_0^2 z^e(t) \right] = -e \overrightarrow{E}(z,t) + \overrightarrow{F}^{ion}(t), \tag{4}$$

where z^e is the displacement of the electron in the z-direction from its equilibrium position, m^e is the mass of the electron, ω_0 is the binding frequency and γ is the damping constant. Considering the contribution of both free and bound electrons to the dielectric constant in the absence of the ionic mechanical force $\overrightarrow{F}^{ion}$, the dispersion relation of gold can be expressed using the following Drude–Lorentz model:

$$\varepsilon(\omega) = \varepsilon_0 - \frac{\omega_D^2}{\omega(\omega + i\gamma_D)} - \frac{\omega_L^2 \Delta \varepsilon}{(\omega^2 - \omega_L^2) + i\gamma_L}, \tag{5}$$

where ε_∞ is the contribution of all the other dipoles, ω_D is the Drude binding frequency, γ_D is the Drude damping constant, ω_L is the Lorentz binding frequency, γ_L is the Lorentz damping constant and $\Delta \varepsilon$ is the weighting factor. The fitted parameters of the Drude–Lorentz model (Vial et al. [48]) are from the experimental values of Johnson and Christy [49] $\varepsilon_\infty = 5.967$, $\omega_D = 13.28 \times 10^{15}$, $\gamma_D = 100.03 \times 10^{12}$, $\omega_L = 4.084 \times 10^{15}$, $\gamma_L = 658.5 \times 10^{12}$ and $\Delta \varepsilon = 1.09$.

The effect of ion collision on the dielectric constant can then be accounted for by adding the external mechanical force $\overrightarrow{F}^{ion}$ to the right side of Eq. (4). The external mechanical force $\overrightarrow{F}^{ion}$ can be described as follows:

$$\overrightarrow{F}^{ion}(t) = -\sum_i \overrightarrow{z} F_i^{ion}(t - t_i), \tag{6}$$

$$F_i^{ion} = \begin{cases} f^{ion} \sin \frac{3\pi(t - t_{i_1})}{t_{i_2} - t_{i_1}}, & t_{i_1} < t < \frac{t_{i_2}}{3} \\ 2f^{ion} \sin \frac{3\pi(t - t_{i_1})}{t_{i_2} - t_{i_1}}, & \frac{t_{i_2}}{3} < t < \frac{2t_{i_2}}{3} \\ f^{ion} \sin \frac{3\pi(t - t_{i_1})}{t_{i_2} - t_{i_1}}, & \frac{2t_{i_2}}{3} < t < t_{i_2} \\ 0, \text{Otherwise} \end{cases} \tag{7}$$

where f^{ion} is the peak amplitude of the ionic thermal force. The simplified configuration of the unit external force of the ith ion F_i^{ion} exerted on the gold wall is shown in Fig. 3A. As shown in Fig. 3A, it has not only $-z$ directional forces (originating from the thermal force of the ion), but also $+z$ directional forces (due to the electrostatic interaction between the ion and electron). The interval of time over which F_i^{ion} acts is $t_{i_2} - t_{i_1} = \tau$, and τ usually ranges from tens of nanoseconds to microseconds. This term can be determined from the number of ions flowing through an open K$^+$ ion channel (10^6 s^{-1}) and the channel height (12 nm). Using the microscopic model of an ideal gas [50], the amplitude can be obtained for the thermal force f^{ion} acting on the wall of a cylinder with height L and bottom surface of gold

$$f^{ion} = \frac{m^{ion} \overrightarrow{v}_z^2}{L}, \tag{8}$$

where m^{ion} is the mass of the ion and $\overrightarrow{v}_z$ is the z component of the ion velocity (12×10^{-3} m/s). The solution of the consecutive Eqs. (4), (6), (7) and (8) was numerically computed using the Green's method (see Eq. (S1) in the Supporting Material).

2.3. Generation of the SPR signal from activated K$^+$ ion movement: independence from electrical noise

To determine the external mechanical force $\overrightarrow{F}^{ion}$, which is a superposition of the unit external mechanical forces F_i^{ion}, the series of ionic collisions should be theoretically estimated using the proper assumptions. In the aCSF region, the significant ions are K$^+$, Na$^+$ and Cl$^-$ ions [51], but the negative charge at the surfaces of the nerve decreases the anion concentrations near the channel entrances [52]. As shown in Fig. 4B, the solution to the PB equation (see Eq. (10)) at a fixed resting nerve extracellular potential of -60 mV shows that the concentration of counterions is more than 100 times greater than the concentration of anions near the nerve membrane and 25 times greater near the gold surface. Therefore, the effects of the counterions (K$^+$ and Na$^+$ ions) are found to be important. Here, the postulation can be done such
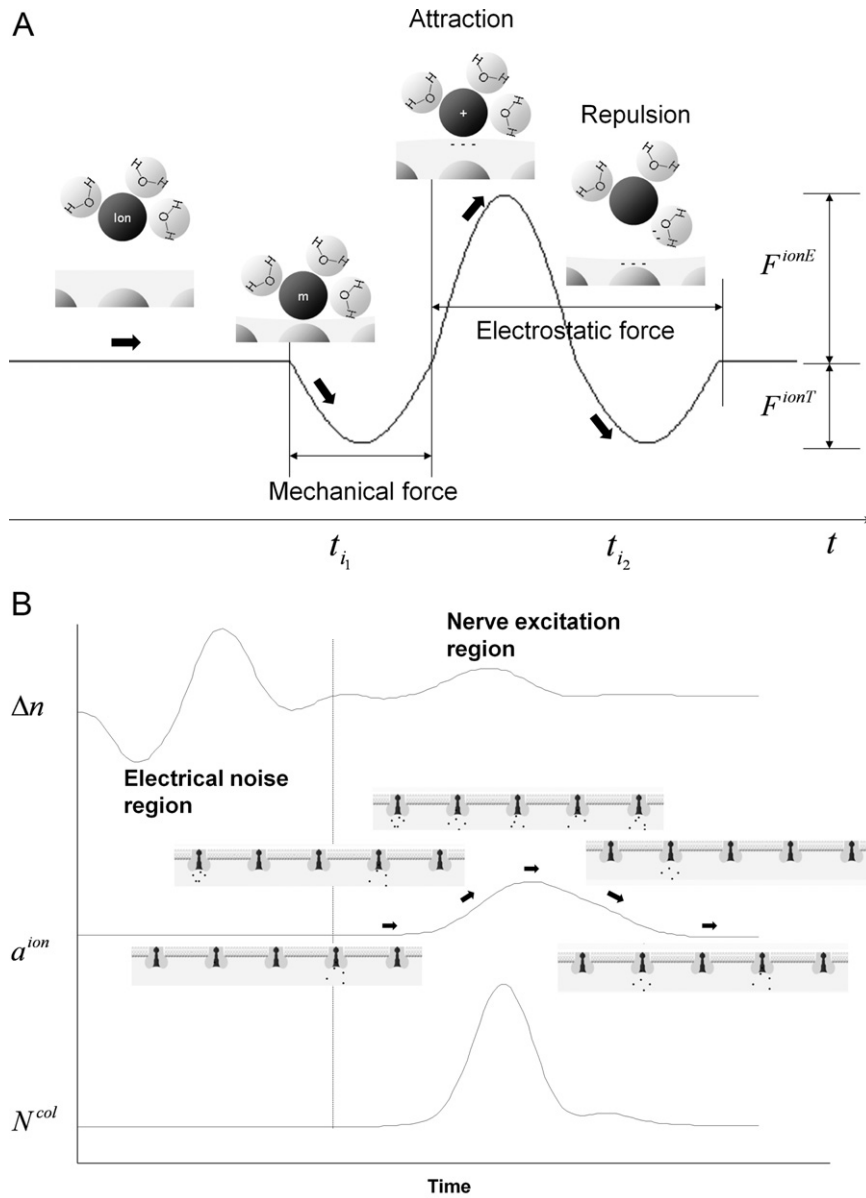
Fig. 3. (A) The modeled cycle of the interaction force between an ion-water molecule cluster and an electron placed around the gold atom during collision. The hydrated ion bounced off the gold atom and exerted a force on its electrons during time τ, which varied for each ion. When the ion-molecular cluster was far from the gold surface, they could not deform the electron fluctuation near the gold atom. The thermal pressure of the hydrated ion then altered the distribution of the gold electron with the force f^{ion}, due to the velocity $\vec{v}_z$ of the hydrated ion and its mass m^{ion}. After thermal pressure, the electrostatic force dominated the motion of the electron. The positive polarity of the ion attracted the gold electron to the $+z$ direction with the force $2f^{ion}$. As the ion moved far from the electron, the negative polarity of the water molecule exerted a pulling force, f^{ion}, on the electron in the $-z$ direction. (B) The number of colliding ion N^{col} as function of time, which was determined by multiplying the change in ion density, Δn, by the activity coefficient, a^{ion}. The ion activity a^{ion} only existed during excitation of the nerve. The a^{ion} was used to describe the portion of ions engaged in motion, which was related to the K^+ ion efflux rate. This parameter originated from changes in various electrically controlled channel states. The coefficient ranged from 0 to 1, where a value of 1 represents the maximum open state of the K^+ ion channel.

that the concentration of counterions near the gold surface is defined by the intermolecular forces between the counterions and gold atoms. Typically, the motion of whole hydrated ions is viscous and constant collisions with surrounding molecules (e.g., water molecules) slow down the overall motion of the hydrated ions [53]. Therefore, the motion of K^+ ions near the ion channel, which is initiated by a jet force of K^+ ions due to nerve excitation, can be distinguished from that of Na^+ ions, which are relatively stable, in the aCSF region. To describe the distinguished motion of K^+ ions, a dimensionless variable is introduced: the coefficient of ion activity a^{ion}, which ranges from 0 to 1. Fig. 3B presents the waveform of the ion activity a^{ion}, which is determined based on the K^+ conductance

through the K^+ ion channel during an action potential. Then, if the change in ion concentration $\Delta n(t, z)$ is equal to $n(t_0, z) - n(t, z)$, where $n(t_0, z)$ is the ion concentration of the resting extracellular potential and $n(t, z)$ is the ion concentration at time t, the temporal average distribution of the number of colliding ions N^{col} can be found as follows (considering the bouncing motions of the ion, the actual distribution of N^{col} would be discrete):

$$N^{col} = a^{ion}\Delta n. \tag{9}$$

Fig. 3B shows the N^{col} curve, which was obtained by multiplying Δn by the activity coefficient a^{ion}. Using this approach, it is obvious that the signal from the electrical noise is not included in the right
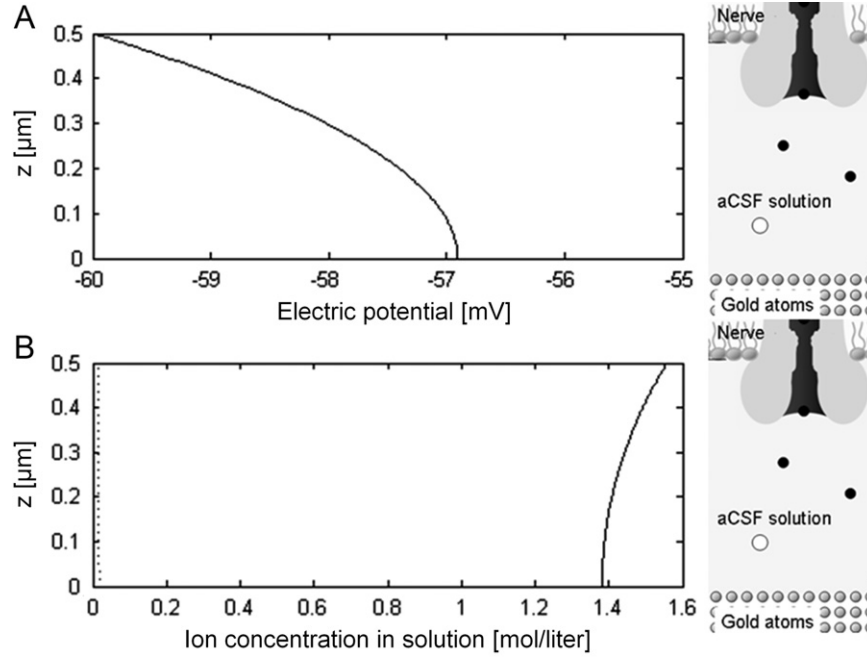
Fig. 4. The z directional (A) electrostatic potential and (B) ion density profiles at a fixed resting nerve's recorded extracellular potential u_m of −60 mV. The solid line is the counter ion density and the dashed line is the anion density.

side of Eq. (4). In other words, this interpretation successfully explains the electrical noise-free characteristic of the SPR neural signal.

2.4. Numerical computation of changes in the ion concentration in the aCSF region during neural activity

From Eq. (9), it is obvious that the number of ionic collisions N^{col} is proportional to Δn. The well-known Poisson–Boltzmann (PB) equation can be used to provide information about the recorded extracellular potential modulated Δn in the aCSF region. According to the Poisson equation, the relationship between the distribution of the charge density $\rho(z)$ (C/m^3) in the z direction and the electric potential $u(z)$ is described as follows:

$$\varepsilon \frac{\partial^2 u(z)}{\partial z^2} = -\rho(z), \tag{10}$$

with $\varepsilon = \varepsilon_0 \varepsilon_r$ (where ε_r is the dielectric constant for aqueous solution, 77.8 at 300 K and 0.1 MPa [44], which is the same condition used in the experiment). For the charge density in solution, the summation should be solved for the charges carried by N different species of ions

$$\rho_e(z) = \sum_{i=1}^{N} z_i e n_i, \tag{11}$$

with

$$n_i = n_{\infty,i} \exp\left(-\frac{z_i e u(z)}{k_B T}\right). \tag{12}$$

Eq. (12) is the Boltzmann distribution for ion density, which has an exponential relationship with the potential of the ion sea. k_B is the Boltzmann constant (1.381×10^{-23} J K^{-1}), T is the medium temperature, e is the element charge (1.602×10^{-19} C), n_i is the number density of each ion, $n_{\infty,i}$ is the number density of each ion in bulk and z_i is the valence of each ion. By combining Eqs. (10)–(12), the following boundary value problem was found for the PB equation, which includes the K$^+$ ion distribution in

the aCSF solution:

$$\frac{\partial^2 u(z)}{\partial z^2} = -\frac{1}{\varepsilon} \sum_{i=1}^{N} z_i e n_{\infty,i} \exp\left(-\frac{z_i e u(z)}{k_B T}\right), \quad z \in \Omega, \tag{13}$$

where Ω is the domain of the aCSF solution region. Since the top side of the boundary is in contact with the nerve, which has fixed extracellular potential u_m, and the bottom side of boundary is in contact with the gold substrate, which has a fixed surface charge density σ (C/m^2), the Dirichlet boundary condition should be used on the top side and the Neumann boundary condition should be used on the bottom side. Therefore, the following boundary conditions were obtained:

$$u(z) = u_m, \quad z \in \partial^{top}\Omega, \tag{14}$$

$$\varepsilon \frac{\partial u(z)}{\partial z} = \sigma, \quad z \in \partial^{bottom}\Omega. \tag{15}$$

The various ion compositions and concentrations in the aCSF were set to be same condition of experiment 150 mM for Na ion, 3 mM for K ion, 1.4 mM for Ca ion, 0.8 mM for Mg ion, 1.0 mM for P ion and 155 mM for Cl ion [51]. The FEM was formulated to get the numerical solution of above boundary value problem (see Eq. (S5)).

3. Results and discussion

3.1. Prediction of the number of ions colliding on the gold surface

The change in ion concentration is first presented in the gap between the nerve and gold surface (aCSF region), which is needed to determine the number of counterions that collide (Eq. (9)) with the gold surface, when the nerve is electrically stimulated with 1 mA current. The recorded electrical signal (see Fig. 1A) was set to the extracellular potential and used for the Dirichlet boundary condition (Eq. (14)). In the experiment, the recording electrode was placed in the extracellular space [4] and used to record the extracellular potential, which was proportional to the second

derivative, with respect to the y-coordinate, of the transmembrane potential [54] or membrane current.

Fig. 4A shows the z directional profile of the electrostatic potential determined from the numerical solution of the PB equation using the Dirichlet boundary condition with a resting nerve extracellular potential of -60 mV at $z=0.5$ μm. In the resting state, the electrostatic potential increases from -60 to -56.9 mV as the distance from the nerve membrane increases. Fig. 4B shows the vertical distribution of the ion density in the aCSF region calculated from the z-directional PB electrostatic potential profile. The solid line is the density of the monovalent counterion (e.g. Na$^+$ ion and K$^+$ ion); and the dashed line is the density of the monovalent anion (e.g. chloride). In the resting state, the molarity of the monovalent counterion decreases from 1.557 to 1.381 mol/l as the distance from the nerve membrane increases. In contrast, the anion concentration near the nerve membrane has a value between 0.015 and 0.016 mol/l, indicating that the anion concentration is 103.8 and 81.7 times less than the counterion concentration at $z=0.5$ and 0 μm, respectively. Based on these results, it is apparent that the concentration of the anion is much less than that of the counterion in a negatively charged environment; this means the need to investigate only the effects of the counterion concentration on the rest of our model equations presented in Section 2.

Time-varying z-directional potential distribution was calculated. Fig. 5A shows the PB electrostatic potentials as a function of time when the Dirichlet boundary condition was used with a recorded extracellular potential u_m, whose waveform is given in the box of Fig. 1A. From this analysis, the overall variations in the electrostatic potential distribution as a function of time in the aCSF region are proportional to the amplitude of a recorded extracellular potential u_m.

Since the number of K$^+$ ions required to generate a transmembrane potential is typically very small [55], the ion concentration in the extracellular space was set at a fixed value while the nerve was fired. This assumption would allow to analyze the change in counterion concentration, Δn, near the gold surface from the decrease in the electrostatic potential. Fig. 5B shows the z-directional change in Δn when the membrane is electrically stimulated. It is worth noting that the counterions, which are placed near the membrane, diffuses into the bottom space of the

model area when the recorded extracellular potential u_m increases or when the $+z$ directional electrical attraction force decreases. Thus, the amplitude of Δn is proportional to the recorded extracellular potential u_m. As shown in Fig. 5B for the maximum u_m the change in ion concentration increases to $\Delta n=0.0025$ mol/l.

As mentioned above in Section 2 (see Fig. 3B), the number of ionic collision, N^{col}, is not solely determined by the Δn, it is also determined by the ion activity function a^{ion}. Based on these simulation results, ions collide with the gold surface only when the nerve is electrically stimulated and the maximum N^{col}, on a 100×100 nm^2 gold surface area can be found during 1 μs, was ~ 15.

3.2. Simulated gold's electron motions are in qualitative agreement with the biphasic oscillation characteristic of the SPR signal

The next analysis was performed on the mechanism behind the biphasically oscillating intensity of reflectance R of Eq. (1), which is the function describing the dielectric constant of the medium in the SPR ATR system. An ionic force was applied to a free and bound electron as illustrated in Fig. 2C, so as to move the electron from its equilibrium state, which in turn induces a change in the average dipole moment $\langle \overrightarrow{p}^{mol} \rangle$ of the gold molecule (see Eq. (4)). The frequency of the ionic force was sufficiently small compared to that of the electric field of light generating the SP; thus, the general effects of the low frequency forces on the free and bound electron motion are simulated.

Fig. 6A shows the numerical solution of Eq. (4) or the instantaneous motion of the free electron whose ω_0 was set at 0. The $+z$ directional electric field initiates the oscillation of free electrons at the same frequency as the electric field and localize free electron to a Tomas–Fermi length $d^{TF} \approx 0.1$ nm. The calculations correspond fairly well with other theoretical studies [1,56,57]. An artificial force was generated parallel to the electric field that is equivalent to the ionic force. This Mexican hat like ionic force function (gray line) evenly distorted the base line of the free electron fluctuations Δz^e. From Eq. (3), the distortion of the base line Δz^e means the change of the temporal average dipole moment $\langle \overrightarrow{p}^{mol} \rangle$ and the dielectric constant of the gold film. Thus, the evenly distorted base line of the free election fluctuations caused by ion–electron collision is the reason why the $\Delta 0R$ fluctuates evenly in a biphasic manner.

If the duration of the base line distortion is sufficiently long comparable to the cut off frequency of the photodiode (≈ 1 MHz), the distorted dipole moment can be detected by optical devices; light typically induces dipole moment changes have very short life times (≈ 10 fs) and the detected dipole moment is the microsecond averaged value [47]. As mentioned above in Section 2, the change in reflectance $\Delta 0R$ was monitored at a fixed angle. The $\Delta Re(\varepsilon_1)/Re(\varepsilon_1)$ can be calculated using Eqs. (1) and (7). These calculations show that the changes in the dipole moment relative to its initial value $\Delta p/p$ correspond to the changes in $\Delta 0R$. This relationship is almost linear and the change in $\Delta 0R=4 \times 10^{-5}$ corresponds to the changes in $\Delta Re(\varepsilon_1)/Re(\varepsilon_1)=6.2 \times 10^{-4}$ and $\Delta p/p=3.05 \times 10^{-5}$. Also, the numerical result of Eq. (4) shows that a $f^{ion}=5.26 \times 10^{-2}$ fN results in compatible change in $\Delta p/p=3.05 \times 10^{-5}$.

Fig. 6B shows the motions of the bound electron. Compared to the motion of the free electron, the bound electron has the binding frequency ω_0 due to a restitution force. For the electrical force of the light, the bound electron starts to oscillate with an amplitude of the 4×10^{-2} pm from its initial position $z=0$. The same ionic force used in Fig. 6A also distorts the dipole moment of gold atom. However, in this case, the amplitude of the distortion is 490 times smaller than that of the free electron. This shows that the dielectric constant change of the gold film induced by the distorted motion of the bound electron is negligible compared to that of the free electron.
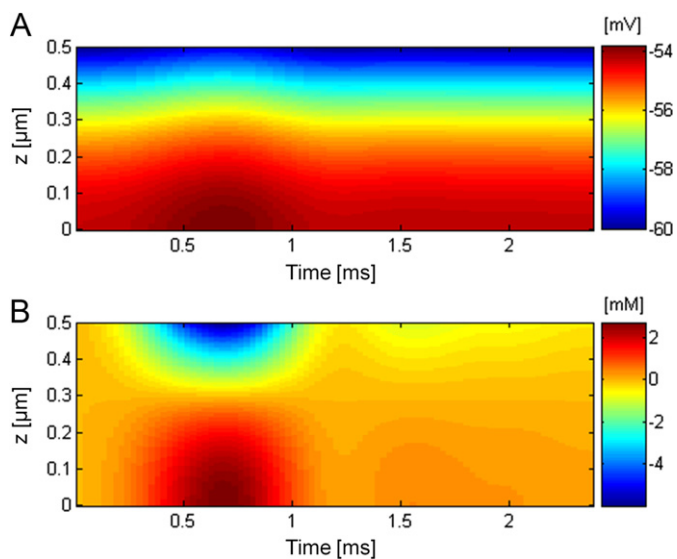

Fig. 5. The z directional (A) electrostatic potential as a function of time and (B) Δn profiles during the action potential.
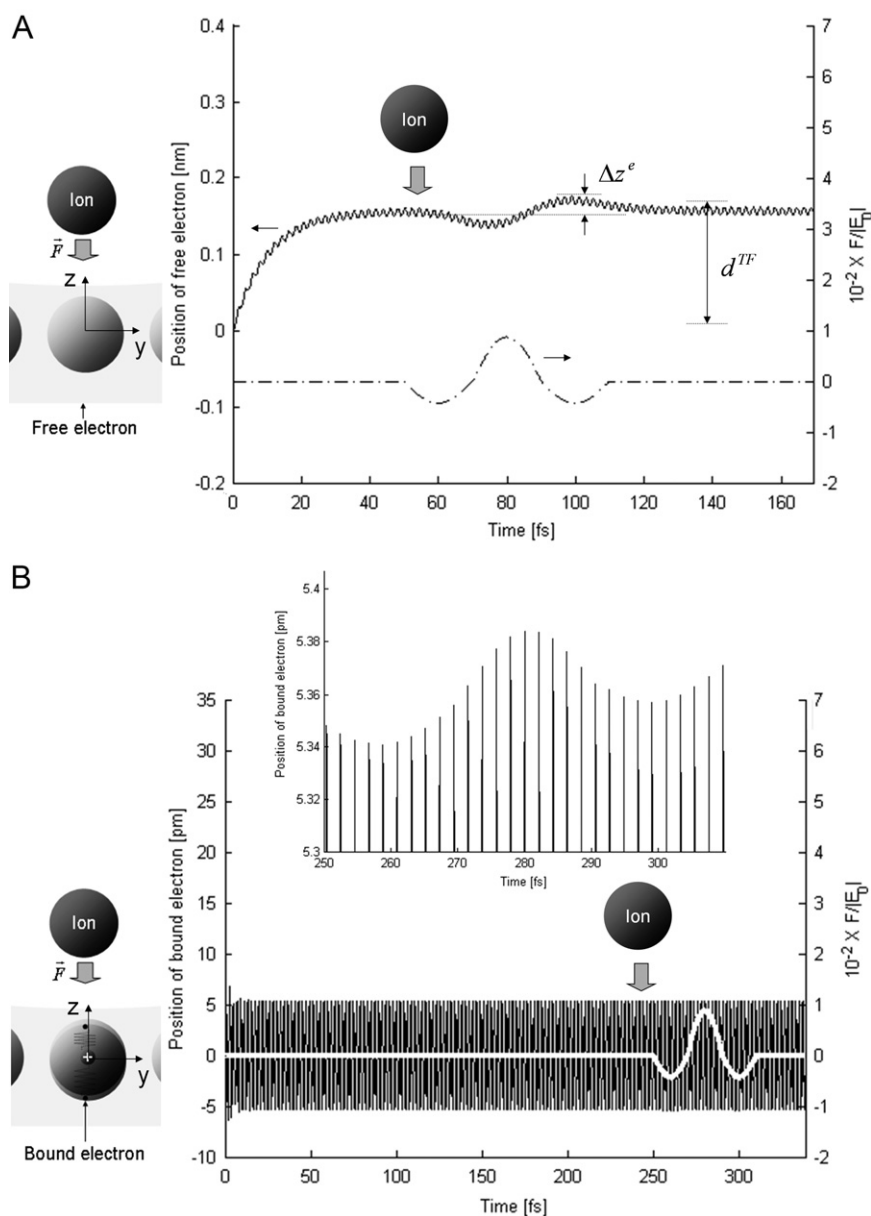
Fig. 6. The computed motions of (A) the free electron and (B) the bound electron, under the combined external electric $\vec{E}$ and ionic $\vec{F}^{ion}$ force. The dashed line represents the ionic force $\vec{F}^{ion}$ and the solid line represents the position of the electron. The ion collides with (A) the free electron at $t=50$ fs and (B) bound electron at $t=250$ fs.

Therefore, the change in $\Delta 0R$ can be attributed mainly to the displacement of the free electrons rather than bound electrons from the gold film.

3.3. The effect of the multiple ionic collisions on the movement of free electrons in gold

Supplementary numerical simulations were conducted for the free electron to investigate the effects of the number of colliding ions N^{col} per unit time on changes in the dipole moment. Fig. 7 shows the displacement of free electrons after 10 consecutive collision events with ions at various time steps Δt_{i_1}. To easily perceive the relative Δt_{i_1} compared to the duration of unit ionic force τ, the time step was divided by the duration of the ionic collision $\Delta t_{i_1}/\tau$.

In the case of $\Delta t_{i_1}/\tau = 0$ (see Fig. 7A), the 10 elemental forces completely overlap without any loss and they produce the strongest change in electron displacement. In the case of $\Delta t_{i_1}/\tau = 0.071$ (see Fig. 7B), the elemental forces slightly overlap and only relatively small changes in electron displacement are observed over longer time periods. In the case of $\Delta t_{i_1}/\tau = 0.212$ (see Fig. 7C), the elemental forces destructively overlap with severe losses from $t=200$ to 250 fs. Under these conditions, the weakest change in electron displacement is observed; it is close to zero. In the case of $\Delta t_{i_1}/\tau = 0.48$ (see Fig. 7D), half of each elemental force overlap, and they generate constitutive sinusoidal waves, whose frequency is smaller than the unit force function. In addition, fluctuations in electron displacement are 10 times greater at this condition.

From these numerical experiments, it can be inferred that the various amplitudes and frequencies of the SPR signal might be dependent on the various force configurations of the multiple ionic collisions, which varies with the time interval of each collision Δt_{i_1} and the duration τ of each unit force function F_i^{ion}.
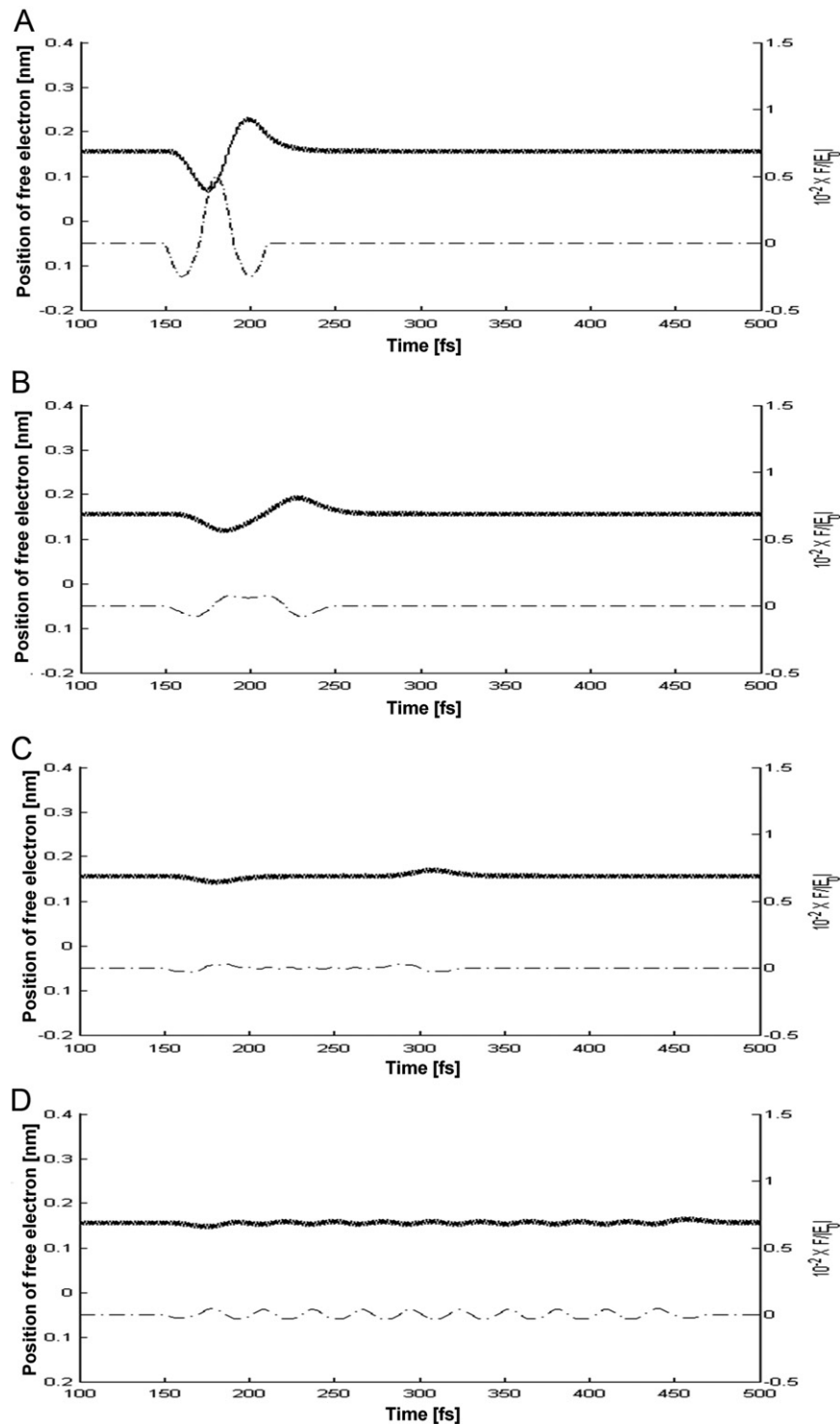
Fig. 7. The computed instantaneous motions of the free electron at various configurations of the ionic forces $\overrightarrow{F}^{ion}$ produced from the superposition of 10 unit ionic forces F_i^{ion} with various time steps. The time intervals divided by collision duration $\Delta t_{i_1}/\tau$ were (A) 0, (B) 0.071, (C) 0.212 and (D) 0.48. For details, see text.

4. Conclusion

A novel hybrid model is proposed for the SPR neural recording system; it accounts for reflectivity changes in a three-layer system, the ionic distribution in the charged area and one-dimensional electron dynamics. A set of numerical simulations, which are related to the fundamental physical phenomenon of the SPR neural recording procedure, was performed. After examining the ionic force curve,

the redistribution of ion concentration and activity coefficients were quantified and the effect of the recorded extracellular potential u_m on the amplitude of the oscillating SPR signal was studied. The effect of the external ionic force on the dynamics of gold electrons was then simulated for the purpose of determining the relationship between the change in the recorded extracellular potential u_m and the dielectric constant of gold or the change in $\Delta 0R$. Moreover, simulations using multiple collisions between ions, which generated the average dipole

moment change in the molecule, were shown to replicate and explain the biphasic nature of the oscillating SPR neural signal at a non-uniform frequency.

However, there are some limits in the proposed model. The first limit of the model concerns the physiological aspect. A realistic quantitative model of the rat sciatic nerve was not fully formulated to study the real kinetics of rat K^+ ion channels. This was not done because the main objective of this study is to describe the relevant mechanical effects of different parameters on the general pattern of channel gating. Second, a rather simple ionic movement was assumed; the average velocity of the counterions $\vec{v}_z$, the configuration of force function $\vec{F}^{ion}$ and its amplitude f^{ion} are currently under study. If adequate realistic molecular dynamic (MD) simulations can be conducted, more reliable information about the ionic movement would be obtained. Lastly, a three-layer system was employed to calculate the reflectance instead of a five-layer system, which would additionally include a nerve layer and upper aCSF region. This was chosen because of the current interest in assessing changes in the reflectance due to changes in the properties of the gold layer. When the limits mentioned above are properly accounted for, the present preliminary model can be refined and become more realistic.

Despite these limits, the most significant result of the analysis in this paper is the assessment of the thermal effects of the extra-cellular ion on the SPR system, which was achieved by connecting unrelated physical phenomena identified in other fields of science. This approach makes it possible to analyze the noise-like $\Delta 0R$ changes induced by molecular pressure and by electrostatic attraction/repulsion forces of the molecules, which can modify the dipole moment of the gold atom.

Further complementary analysis on some of the features of the present quantitative model is still needed to further understand all the parameters that affect the generated changes in SPR signals; nevertheless, several key features have been reasonably described by the present work.

Acknowledgements

Appendix A. Supplementary material

Supplementary data associated with this article can be found in the online version at doi:10.1016/j.optlastec.2010.12.010.

References

[1] Reather H. Surface plasmons on smooth and rough surfaces and on gratings. Berlin: Springer-Verlag; 1986.
[2] Prigogine I, Rice SA. Advances in chemical physics. New York: Wiley; 1983.
[3] Knoll W. Interfaces and thin films as seen by bound electromagnetic waves. Annu Rev Phys Chem 1998;49:569–638.
[4] Kim SA, Byun KM, Lee J, Kim JH, Kim D-GA, Baac H, et al. Optical measurement of neural activity using surface plasmon resonance. Opt Lett 2008;33:914–6.
[5] Hill DK, Keynes RD. Opacity changes in stimulated nerve. J Physiol 1949;108:278–81.
[6] Cohen LB, Keynes RD, Hille B. Light scattering and birefringence changes during nerve activity. Nature 1968;218:438–41.
[7] Cohen LB, Keynes RD, Landowne D. Changes in light scattering that accompany the action potential in squid giant axons: potential-dependent components. J Physiol 1972;224:701–25.
[8] Cohen LB, Keynes RD, Landowne D. Changes in axon light scattering that accompany the action potential: current-dependent components. J Physiol 1972;224:727–52.
[9] Tasaki I, Byrne PM. The origin of rapid changes in birefringence, light scattering and dye absorbance associated with excitation of nerve fibers. Jpn J Physiol 1993;43:S67–75.
[10] Huang D, et al. Optical coherence tomography. Science 1991;254:1178–81.
[11] Fercher AF, Drexler W, Hitzenberger CK, Lasser T. Optical coherence tomography—principles and applications. Rep Prog Phys 2003;66:239–303.
[12] Bonhoeffer T, Grinvald A. Optical imaging based on intrinsic signals. London: Academic Press; 1996.
[13] Yao XC, Yamauchi A, Perry B, George JS. Rapid optical coherence tomography and recording functional scattering changes from activated frog retina. Appl Opt 2005;44:2019–23.
[14] Gratton G, Corballis PM. Removing the heart from the brain: compensation for the pulse artifact in the photon migration signal. Psychophysiology 1995;32:292–9.
[15] Rector DM, Poe GR, Kristensen MP, Harper RM. Light scattering changes follow evoked potentials from hippocampal Schaeffer collateral stimulation. J Neurophysiol 1997;78:1707–13.
[16] Rector DM, Rogers RF, Schwaber JS, Harper RM, George JS. Scattered-light imaging in vivo tracks fast and slow processes of neurophysiological activation. NeuroImage 2001;14:977–94.
[17] Rector DM, Carter KM, Volegov PL, George JS. Spatio-temporal mapping of rat whisker barrels with fast scattered light signals. NeuroImage 2005;26:619–27.
[18] Strangman G, Boas DA, Sutton JP. Non-invasive neuroimaging using near-infrared light. Biol Psychiat 2002;52:679–93.
[19] Stepnoski RA, Laporta A, Raccuia-Behling F, Blonder GE, Slusher RE, Kleinfeld D. Noninvasive detection of changes in membrane potential in cultured neurons by light scattering. PNAS 1991;88:9382–6.
[20] Banker G, Goslin K. Culturing nerve cells. Cambridge: MIT Press; 1998.
[21] Grinvald A, Ross WN, Farber I. Simultaneous optical measurements of electrical activity from multiple sites on processes of cultured neurons. Neurobiology 1981;78:3245–9.
[22] Schei JL, McCluskey MD, Foust AJ, Yao XC, Rector DM. Action potential propagation imaged with high temporal resolution near-infrared video microscopy and polarized light. Neuroimage 2008;40:1034–43.
[23] Cooper MA. Optical biosensors in drug discovery. Nat Rev Drug Discovery 2002;1:515–8.
[24] Kawata S. Near field optics and surface plasmon polaritons. Berlin: Springer; 2001.
[25] Wang L, Jacques SL. MCML-Monte Carlo modeling of light transport in multi-layered tissues. Comput Methods Prog Biomed 1995;47:131–46.
[26] Keijzer M, Star WM, Storichi PRM. Optical diffusion in layered media. Appl Opt 1988;27:1820–4.
[27] Prahl SA. Light transport in tissue. Ph.D. thesis. The University of Texas at Austin; 1988.
[28] Qiang R, Wu D, Chen J, Wang S, Wilton D, Kainz W. An efficient two-dimensional FDTD method for bio-electromagnetic applications. IEEE Trans Mag 2006;42:1391–4.
[29] Boas DA, Dale AM, Franceschini MA. Diffuse optical imaging of brain activation: approaches to optimizing image sensitivity. NeuroImage 2004;23:275–88.
[30] Okamoto T, Yamaguchi I, Kobayashi T. Local plasmon sensor with gold colloid monolayers deposited upon glass substrates. Opt Lett 2000;25:372–4.
[31] Svoboda K, Block SM. Biological applications of optical forces. Biophys Biomol Struct 1994;23:247–85.
[32] Novotny L, Bian RX, Xie XS. Theory of nanometric optical tweezers. Phys Rev Lett 1997;79:645–8.
[33] Zhang J, Atay T, Nurmikko AV. Optical detection of brain cell activity using plasmonic gold nanoparticles. Nano Lett 2009;9:519–24.
[34] Kume T, Hayashi S, Yamamoto K. Light emission from surface plasmon polaritons mediated by metallic particles. Phys Rev B 1997;55:4774–82.
[35] Kume T, Hayashi S, Yamamoto K. A new method of surface plasmon excitation using metallic fine particles. Mater Sci Eng A 1996;217/218:171–5.
[36] Hodgkin AL, Huxley AF. A quantitative description of membrane current and its application to conduction and excitation in nerve. J Physiol 1952;117:500–544.
[37] Jackson JD. Classical electrodynamics. 3rd ed.. New York: John Wiley and Sons; 1999.
[38] Marion JB, Thornton ST. Classical dynamics of particles and systems. Fort Worth: Saunders College Publishing; 1988.
[39] Becker EB, Carrey GF, Oden JT. Finite elements an introduction. New Jersey: Prentice Hall; 1981.
[40] Israelachvili J. Intermolecular and surface forces. New York: Elsevier; 1992.
[41] Kim D, Darve E. Molecular dynamics simulation of electro-osmotic flows in rough wall nanochannels. Phys Rev E 2006;73:051203-1–12.
[42] RefractiveIndex.INFO—Refractive index database. ⟨http://refractiveindex.info⟩ (accessed July 1, 2009).
[43] Palik ED. Handbook of optical constants of solids. Academic Press; 1998.
[44] Raton B. CRC handbook of chemistry and physics. CRC Press; 2006.
[45] Beiser A. Consepts of modern physics. Boston: MC Graw Hill; 2003.
[46] Rosencher E, Vinter B. Optoelectronics. Cambridge: Cambridge University Press; 2002.
[47] Hecht E. Optics. Seoul: Addison Wesley Longman; 2002.
[48] Vial A, Grimault A-S, Macias D, Barchiesi D, de la Chapelle ML. Improved analytical fit of gold dispersion: application to the modeling of extinction spectra with a finite-difference time-domain method. Phys Rev Lett 2005;71:085416-1–6.

[49] Johnson PB, Christy RW. Optical constants of the noble metals. Phys Rev B 1972;6:4370–9.

[50] Schroeder DV. An introduction to thermal physics. San fransisco: Addison-wesley; 2000.

[51] ALZET® Pump Models. ⟨http://www.alzet.com/products⟩ (accessed July 1, 2009).

[52] Bostrom M, Williams DRM, Ninhamy BW. Specific Ion effects: why the properties of lysozyme in salt solutions follow a hofmeister series. Biophys J 2003;85:686–94.

[53] Glaser R. Biophysics. Berlin: Springer; 2001.

[54] Plonsey R, Barr RC. Bioelectricity a quantitative approach. New York: Kluwer Academic/Plenum Publishers; 2000.

[55] Malmivuo J, Plonsey R. Bioelectromagnetism. Oxford: Oxford University Press; 1995.

[56] Davis D. Thomas-fermi screening in one dimension. Phys Rev B 1973;7: 129–35.

[57] Fenn JB, Rawlings PK. Solution of the thomas-fermi problem for continuous, spherical, positive charge distribution. J Stat Phys 1973;8:335–9.

[58] Water (properties)—Wikipedia, the free encyclopedia. ⟨http://en.wikipedia.org/wiki/Water_(molecule)⟩ (accessed July 1, 2009).

[59] Gold—Wikipedia, the free encyclopedia. ⟨http://en.wikipedia.org/wiki/Gold⟩ (accessed July 1, 2009).

[60] Brismar T. Potential clamp analysis of membrane currents in rat myelinated nerve fibres. J Physiol 1980;298:171–84.

[61] Kandel ER, Schwartz JH, Jessell TM. Principles of neural science. New York: McGraw-Hill; 2000.